ChemElectroChem

Research Article
doi.org/10.1002/celc.202200317

Chemistry Europe
European Chemical Societies Publishing

www.chemelectrochem.org

Composite Solid Electrolyte for High Voltage Solid-State Li-Metal Battery

Ramkumar Balasubramaniam,[a] Chan-Woo Nam,[a] Vanchiappan Aravindan,*[b] Jae-chang Seol,[a] Kanalli V. Ajeya,[c] Ho-Young Jung,[c, d] and Yun-Sung Lee*[a]

A composite solid electrolyte (CSE) was prepared by incorporating $Li_7La_3Zr_2O_{12}$ (LLZO) particles, lithium bis(trifluoromethanesulfonyl) imide (LiTFSI), and different concentrations of a solid plasticizer in a poly(vinylidene fluoride hexafluoropropylene) (PVDF-HFP) matrix. Subsequently, we investigated the ionic conductivity and electrochemical stability of the CSE, and its interfacial compatibility with a Li-metal electrode. 30 wt.% plasticizer with CSE exhibits a high ionic conductivity of 4.23×10^{-4} and 8.14×10^{-4} S cm^{-1} at 25 and 60 °C, respectively, with an excellent stability of up to 4.76 V *vs.* Li/Li$^+$. The CSE is sandwiched between the Li-metal and NCM811 for the fabrication of a solid-state battery (SSB), which delivers a discharge capacity (163 mAh g^{-1}) at a rate of 0.2 C (60 °C). The $LiNbO_3$ (LNO) modification over the NCM811 cell delivers a high discharge capacity of 198 mAh g^{-1}, excellent rate capability, and good cycle life. Furthermore, the LNO coating on the surface of the NCM811 cathode, which effectively improves the contact between the cathode and electrolyte, eventually leads to an increase in the discharge capacity. Therefore, the prepared CSE is a good choice for use in SSB; moreover, the LNO coating noticeably improved the cycling stability, reversibility, and rate capability compared to an unmodified NCM811 cathode in the SSB configuration.

Introduction

Rechargeable lithium-ion batteries (LIBs) are considered state-of-the-art battery technology for use in electronic gadgets, such as cell phones, laptops, tablets, other portable devices, and electric vehicles owing to their high energy density, extended life cycle, low self-discharge, no memory effect, lightweightness, and a high operating potential.[1–4] However, conventional LIBs continue to experience safety hazards, including Li dendrite formation, explosions initiated by flammable organic solvents, electrolyte leakage, and unwanted side reactions.[5–6] Employing solid electrolytes in the fabrication of the next-generation LIBs is one of the most efficient strategies for resolving these challenges.[7] Solid-state batteries (SSB) provide excellent safety features due to the replacement of the flammable organic solvent with Li metal as an anode, which helps realize higher energy density.[8–10] Nevertheless, an ideal solid electrolyte fulfills the following requirements: high ionic conductivity, and good electrochemical and mechanical compatibility with a wide range of electrodes comprised of various redox potentials.[11] Unfortunately, poor electrochemical and mechanical stability between the high voltage cathode and the electrolyte remains a bottleneck for all-solid-state-LMBs (ASSLMB).[12]

In the last two decades, different types of Li-ion superionic conductors have been developed, including garnet, perovskite, NASICON, thiophosphate, and argyrodites based conductors.[13–14] Among the ceramic electrolytes, the garnet type $Li_7La_3Zr_2O_{12}$ (LLZO) and its derivatives have garnered considerable interest owing to their reasonable ionic conductivity (~10^{-3} S cm^{-1}), large electrochemical window (5 V *vs.* Li/Li$^+$), good chemical stability against high voltage cathodes, and good compatibility with Li metal anodes.[15–18] Nevertheless, the brittle nature and large interfacial impedance between the electrode and ceramic electrolyte are the foremost hindrances to practical applications on a large-scale.[15,16,19] Other types of solid polymer electrolytes with matrices, such as polyethylene oxide (PEO), poly(vinylidene fluoride) (PVDF), and poly(vinylidene fluoride-co-hexafluoropropylene) (PVDF-HFP) are flexible and have good compatibility with electrodes; however, practical applications are restricted by their low ionic conductivity at 25 °C.[20–23] To address these shortcomings, composite solid electrolytes (CSEs) are prepared through the incorporation of ceramics into polymer electrolytes by solution casting to attain high ionic conductivity and retain good compatibility.[21,23,24] From among these polymers, PVDF-HFP is predominantly used because of its high dielectric constant (ε = 8.4), which facilitates the dissociation of Li-salts and promotes ionic motion. It contains both amorphous (-HFP) and crystalline phase (-VDF) units. The crystalline phase provides mechanical stability and the amorphous phase assists in increasing the ionic conductivity of the electrolyte.[25–26]

Research on PVDF-HFP/LLZO CSE-based cells has led to significant improvements, such as high ionic conductivity and

[a] R. Balasubramaniam, C.-W. Nam, J.-c. Seol, Y.-S. Lee
School of Chemical Engineering, Chonnam National University, Gwangju, 61186, Republic of Korea
E-mail: leeys@chonnam.ac.kr
[b] V. Aravindan
Faculty of Department of Chemistry, IISER Tirupati-517 507, India
E-mail: aravindan@iisertirupati.ac.in
[c] K. V. Ajeya, H.-Y. Jung
Department of Environment and Energy Engineering, Chonnam National University, Gwangju-61186, Republic of Korea
[d] H.-Y. Jung
Center for Energy system, Chonnam National University, Gwangju-61186, Republic of Korea

Supporting information for this article is available on the WWW under https://doi.org/10.1002/celc.202200317

good capacity; however, additional organic flammable electrolytes are warranted to maintain a good electrode and electrolyte interface.[27–28] In this study, we prepared a CSE using a solid plasticizer to achieve a high ionic conductivity and good electrochemical stability suitable for high voltage electrodes. Consequently, we used succinonitrile (SN) as a plasticizer in the preparation of CSE, which improved the compatibility with electrodes without compromising the ionic conductivity. A plastic crystal, SN, was used as a plasticizer to suppress the crystallinity further and eventually enhance the amorphous nature of the electrolytes.[29,30] Interestingly, SN can also act as an effective ionizer for dissociating Li-ions from Li-salt in addition to the high dielectric PVDF-HFP.[31,32] Previous studies have focused only on the $LiFePO_4$ cathode; however, it has a low redox potential of ~3.4 V *vs.* Li/Li^+.[21,28,33,34] The most promising candidates for the cathode are Ni-rich layered oxides because of their high discharge capacity, higher working voltage, cost-effectiveness, and easier synthesis protocol.[35,36,37] The Ni-rich $LiNi_{0.8}Co_{0.1}Mn_{0.1}O_2$ cathode has rarely been investigated for use in ASSLMB; however, it can attain a high energy density of up to 300 Wh kg^{-1} in a conventional electrolyte.[38]

Surface modifications of the NCM811 cathode during the fabrication of SSB are one of the primary factors in improving the compatibility with a solid electrolyte. Compared with conventional protective coatings (Al_2O_3, MgO, CeO_2, ZrO_2, and Co_3O_4), the $LiNbO_3$ coating certainly improves the electrochemical activity of the cell.[38,39,40] In this study, the $LiNbO_3$ coating not only enhanced the capacity but also ensured better compatibility between the cathode and electrolyte. In the CSE, the inclusion of 30 wt.% plasticizer increased the ionic conductivity, and it displayed good cyclability in a symmetric cell with Li. The Li//LNO-NCM cell with CSE provides a high discharge capacity, cycle life, and rate capability due to increased interfacial contact and suppressed Li-deficiency across the interface, as discussed in detail in the following sections.

Results and Discussion

Physical characterization

Structural analysis

Figure 1a and b shows the schematic diagram of the composite solid electrolyte (CSE) and all-solid-state Li-metal battery (ASSLMB). Figure 2a shows the XRD profiles of the LLZO, PVDF-HFP, and as-prepared CSEs (S0–S4). It can be seen that the peaks are well-matched with the garnet framework in the space group of Ia-3d.[41] The intensity of the LLZO reflections is suppressed due to the formation of the composite with PVDF-HFP and ceramic filler. The broad peak represents the semi-crystalline nature of the CSEs, which signifies the presence of amorphous regions and is anticipated to enhance the ionic conductivity.[42] The FE-SEM image was used to investigate the surface morphology of the LLZO powder and is presented in Figure S1. The morphology of the particle is coarse in nature, and the average size is estimated to be around 5 μm. FT-IR spectroscopy is a powerful tool for investigating the functional

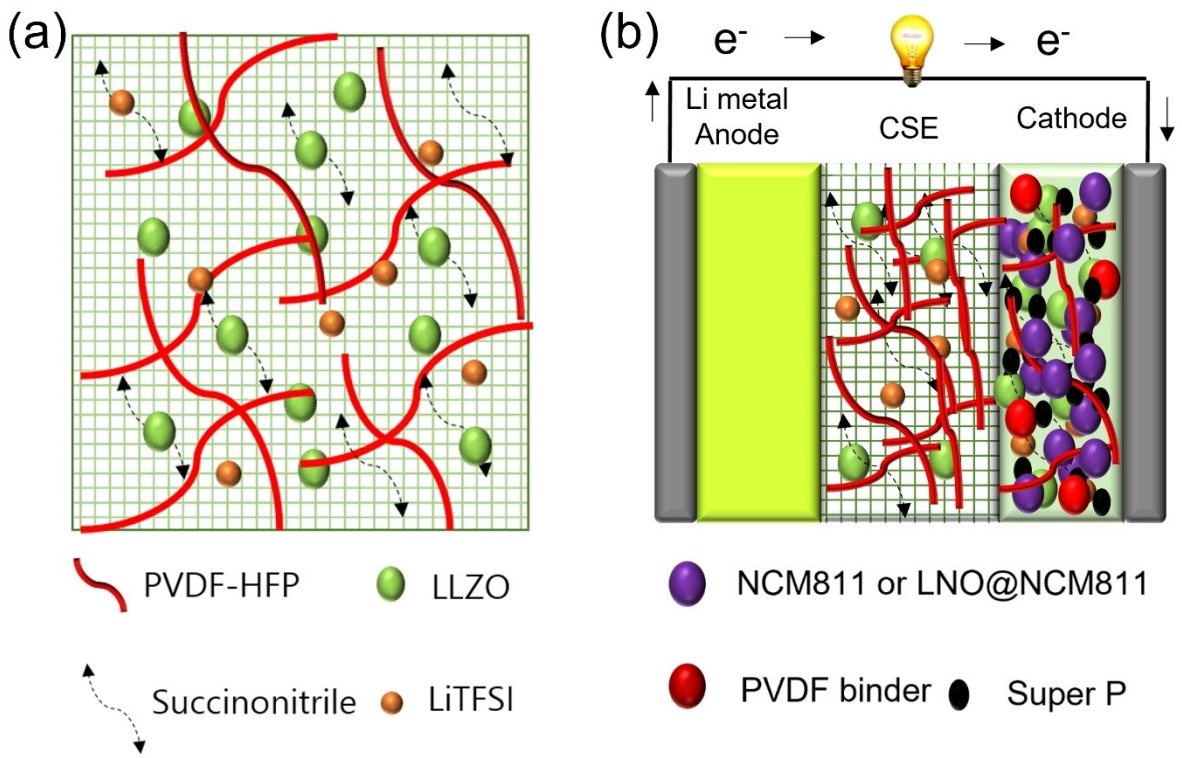

Figure 1. Schematic diagram of (a) composite solid electrolyte, and (b) all-solid-state Li-metal battery (ASSLMB) with NCM or LNO NCM811 composite as a cathode, Li metal as an anode, and a PVDF-HFP-LiTFSI-10% LLZO-30% succinonitrile as a composite solid electrolyte.

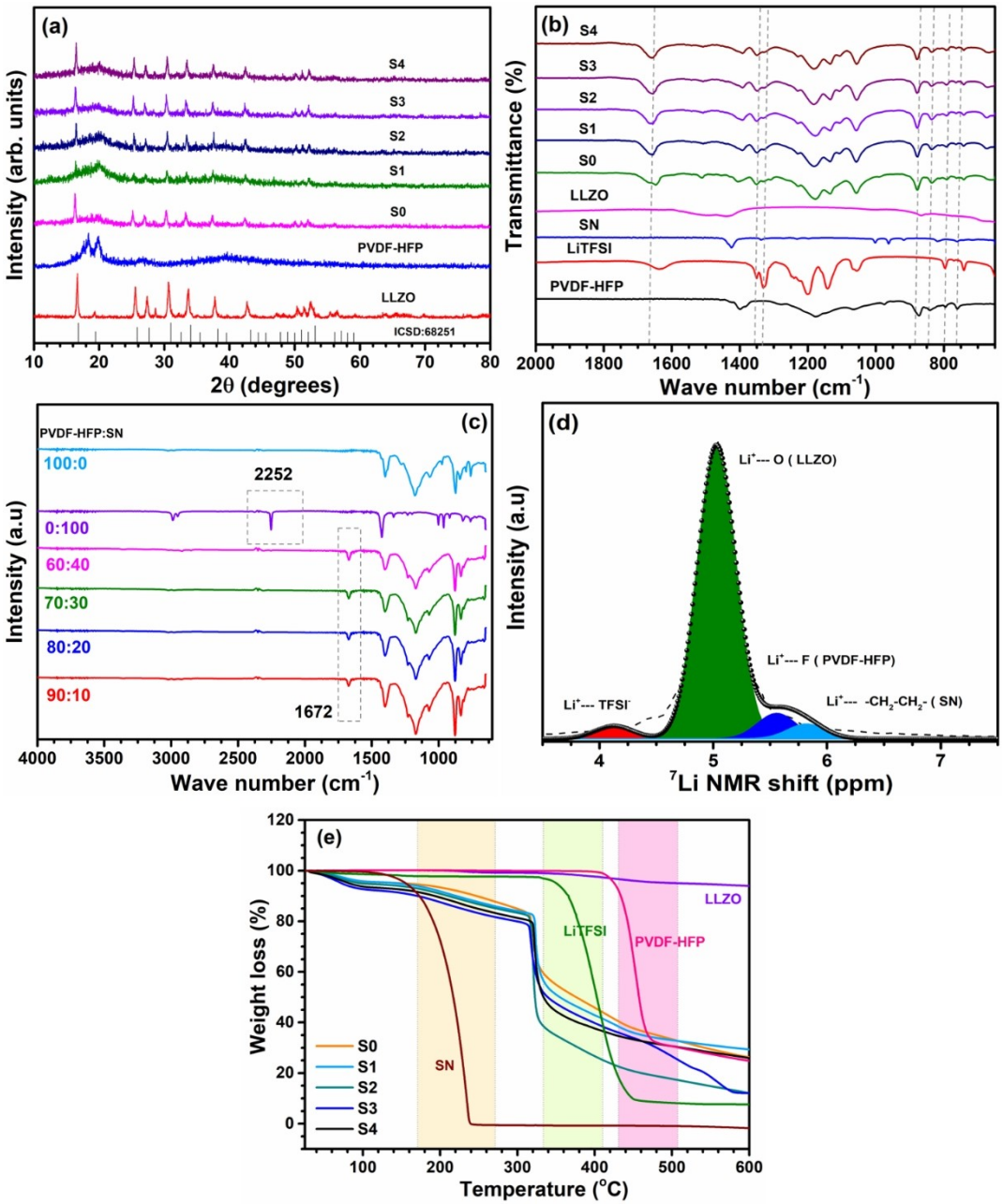

Figure 2. (a) XRD pattern of the LLZO ceramic powder, PVDF-HFP and composite solid electrolytes (S0–S4), (b) Fourier-Transform infrared spectra of the LLZO, succinonitrile, LiTFSI salt, PVDF-HFP, and composite solid electrolytes (S0–S4),(c) FTIR spectra for the PVDF-HFP with different wt% of succinonitrile plasticizer film (without LiTFSI salt), (d) ^{7}Li NMR spectra for the S3 composite solid electrolyte and (e) Thermogravimetric analysis (TGA) curve of the composite solid electrolytes (S0–S4), PVDF-HFP, LiTFSI, SN and LLZO.

groups and complex formation of CSEs (S0–S4). The FTIR spectra of the LLZO, SN, LiTFSI salt, PVDF-HFP, and CSEs are in the range of 4000–400 cm^{-1} and are shown in Figure 2b. PVDF-HFP is a semi-crystalline polymer, therefore, its vibrational spectra contain crystalline (α-phase) and amorphous phase (β-phase) related reflections, for example, the peaks observed at 682, 727, 759, 794, 948, and 974 cm^{-1} are associated with the α-phase, whereas the amorphous peaks (β-phase) are observed at 840 and 873 cm^{-1}.[43] The peaks observed at 759, 794, 840, 873, and 974 cm^{-1} correspond to the CH_2 rocking vibration, CF_3 stretching vibration, mixed-mode of CH_2 rocking, combined CF_2 and CC stretching vibrations, and C–F stretching mode of PVDF-HFP, respectively.[43,44] After the incorporation of LiTFSI salt, SN, and LLZO ceramic filler into the polymer matrix, the crystalline peaks (α-phase) at 682, 727, 759, 794, 948, and 974 cm^{-1} either disappear or become weak, but the amorphous peaks remain prominent and slightly shift position to 835 and 879 cm^{-1}.[43] The two peaks located at 1350 and 1330 cm^{-1} were due to the asymmetric SO_2 vibration mode and C-SO_2-N bond group, respectively.[45,46] The peak shifts and intensity variations

clearly confirms that CSEs contains the polymer backbone, Li-salt, ceramic filler, and plasticizer. In the FTIR spectra (S0–S4), we observe an appearance of a new peak at 1647 cm^{-1} (S0) and 1655 cm^{-1} (S1–S4) corresponding to the double-bonded sulfur with oxygen.[45] This new peak originated owing to the incorporation of the LiTFSI salt in the polymer matrix. The strong sulfur with oxygen (S=O) bond screening the weak intensity bond and further the low-intensity peak was overlapped due to the complex nature of the film (S1–S4). Compared to S0 CSE FTIR spectra (1647 cm^{-1}), the S1–S4 CSE spectra were slightly shifted to the higher wavenumber side (1655 cm^{-1}) due to the incorporation of the succinonitrile (SN) plasticizer. But the FTIR spectra of the PVDF-HFP film with different wt% of succinonitrile (SN) plasticizer (without LiTFSI salt) confirm the bond between the polymer (PVDF-HFP) and plasticizer (SN). Figure 2c shows the FTIR spectra of the PVDF-HFP film with different wt% of succinonitrile (SN) plasticizer. The nitrile group (–C≡N, 2252 cm^{-1}) in the succinonitrile is making a bond with (–CH_2–CF_2, crystalline) –VDF group and the new peak evolved at 1672 cm^{-1} is correlated to increase the amorphous nature of the film.[47] The amorphous of the film is assist to enhance the ionic conductivity and compatibility of the CSE. Figure 2d shows the ^{7}Li NMR spectra for the S3 composite solid electrolyte. The broad and asymmetric resonance peak revealed more than one Li^+ ion local environment present in the CSE. The resonance peak shift and intensity variation are due to the interaction of LLZO particles and LiTFSI salt with PVDF-HFP and SN plasticizer. The interaction induces the structural modification in the PVDF-HFP polymer and provides a new favourable path for fast Li-ion migration (Li^+–F in PVDF-HFP at 5.55 ppm), which enhances the ionic conductivity.[48,49]

Surface morphology

The surface morphology of the pure S0, S1, S2, S3, and S4 CSEs was investigated by FE-SEM. Figure S2 shows a macroscopic image of the large crystalline grains with the lamellar structure, which are evenly distributed in the plasticizer-free electrolyte (S0). After incorporation of SN into the polymer matrix, the size of the grains decreases, and the amorphous nature of the electrolyte grows (see inset of microscopic image Figure S2). After the addition of different wt% SN, CSE loses its crystallinity, and the formation of amorphous parts in the electrolyte is evident from the XRD analysis. [Figure 2a] Improvement in the ionic conductivity is noted with an increase in the amorphous domains in the CSEs.[43,45] The thickness of the CSEs is approximately 200 μm. The energy dispersive spectra images show that the presence of the elements La, Zr, and N are evenly distributed across the mapped area in the CSE. [Figure S3]

Thermal stability

Thermal stability is one of the crucial factors in CSEs for ensuring cell-safety, especially at elevated temperature conditions. Figure 2e shows the thermogravimetric analysis (TGA) of the SN, PVDF-HFP, LiTFSI salt, LLZO ceramic filler, and CSEs, whereby the decomposition events of SN, LiTFSI, and PVDF-HFP start at 150, 330, and 420 °C, respectively.[50–53] The CSEs membrane decomposition through a three-step phase is shown in Figure 2c. In the first phase (150−250 °C), the major weight loss corresponds to the SN plasticizer as they easily decompose compared with the polymer matrix. Once the temperature has reached above 320 °C, sudden weight loss is observed, which is due to LiTFSI decomposition (second phase). Above 420 °C, a third phase of weight loss arises due to PVDF-HFP film decomposition, and the remaining weight corresponds to the LLZO filler. It is well-established that the good thermal stability of the CSEs indicates suitability for Li-ion SSB applications in terms of thermal properties.

PVDF-HFP electrolyte results

The Nyquist plots of the electrochemical impedance spectra (EIS) of the CSEs (S0–S4) at various temperatures are shown in Figures 3 and S4. The Li-ion conductivity of the electrolyte is calculated based on the following formula $\sigma = l/(R_b \times A)$, where l is the thickness, R_b is the resistance which can be measured from the intercept with the X-axis, and A is the area of the electrolyte. Figure 3b illustrates the Arrhenius plot for different wt.% of plasticizer-based PVDF-HFP-LiTFSI-10 wt.% LLZO electrolytes. The addition of the SN plasticizer certainly increases the ionic conductivity in both the low and high-temperature ranges. The main reason for this ionic conductivity enhancement is due to a suppression of the crystallinity in the polymer matrix, which increases the free charge carrier concentration in the electrolyte.[31,54] Among the various compositions prepared, the ionic conductivity of the CSE (S3) sample was calculated to be superior, for example, it was determined to be 4.23×10^{-4} and 8.14×10^{-4} S cm^{-1} at 25 and 60 °C, respectively, with an activation energy of 0.184 eV (Table 1). Initially, we observe that the ionic conductivity of the electrolyte is enhanced with increasing concentration of the plasticizer. After reaching the maximum concentration of 30 wt.%, the increasing trend reversed because of the insulating

Table 1. Ionic conductivity of the CSEs for different wt. % of plasticizers.

Temperature	S0	S1	S2	S3	S4
25	3.93×10^{-5}	7.71×10^{-5}	1.83×10^{-4}	4.23×10^{-4}	1.96×10^{-4}
40	6.87×10^{-5}	1.25×10^{-4}	2.05×10^{-4}	5.91×10^{-4}	3.24×10^{-4}
60	1.3×10^{-4}	2.25×10^{-4}	3.69×10^{-4}	8.14×10^{-4}	5.91×10^{-4}
80	2×10^{-4}	3.51×10^{-4}	4.79×10^{-4}	1.33×10^{-3}	8.46×10^{-4}

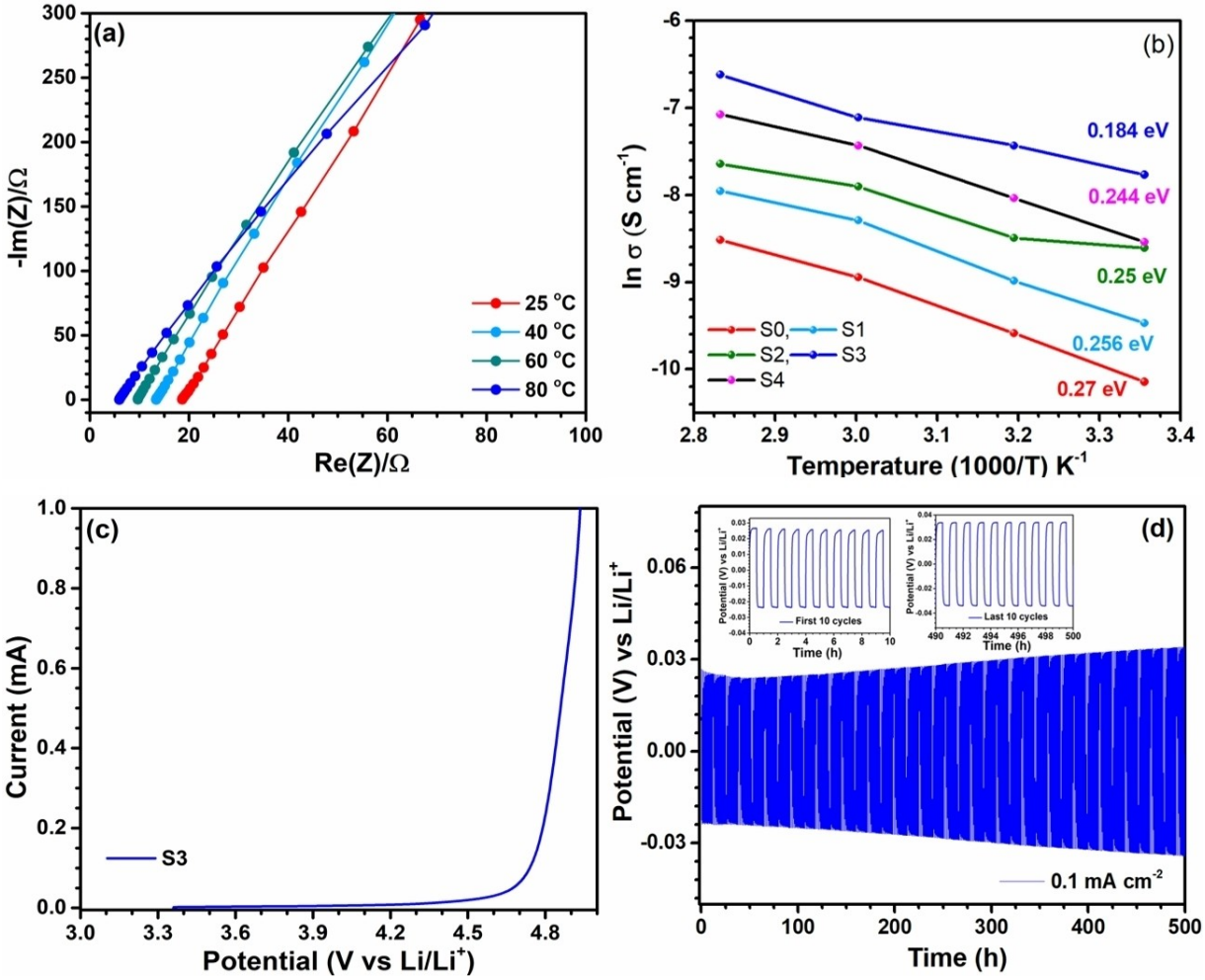

Figure 3. (a) Electrochemical impedance spectra (EIS) curve of the SS||S3||SS cell, (b) Arrhenius plot of the S0–S4 electrolytes, (c) linear sweep voltammetry (LSV) curve of asymmetric Li||S3||SS cell and (d) galvanostatic-charge/discharge curve (GCD) of the symmetric Li||S3||Li cell. The electrochemical performance was studied at 60 °C.

behavior of the non-ionic plastic crystal (SN) and weakened interactions between the plasticizer and Li-ions.[31,55] Therefore, the high ionic conductive S3 electrolyte is used for further electrochemical analysis. For comparison, we tested the ionic conductivity of the 20 and 30 wt. % LLZO based composite solid electrolytes. After more than 10 wt%, the ionic conductivity of the electrolyte is decreased due to the agglomeration of the LLZO particles (Figure S5). The FE-SEM images of the 20 and 30 wt% LLZO based CSEs confirm the agglomeration of the LLZO particles (Figure S6). Figure S7 shows the chronoamperometry (CA) curve of the S3 electrolyte Li-symmetric cell and its Li-ion transference number t_{Li+} is 0.406. The potential stability of S3 was studied by linear sweep voltammetry (LSV) at 60 °C. Figure 3c shows that the S3 electrolyte was stable up to 4.76 V *vs.* Li/Li^+ because of a good incorporation between the LLZO, LiTFSI, and PVDF-HFP matrix. This result indicates that the CSE is appropriate for use in SSB applications, especially while paired with high voltage cathodes such as NCM811 and metallic Li. To further understand the electrochemical Li-plating and stripping behavior, a symmetric cell (Li|S3|Li) was fabricated and studied galvanostatically at 60 °C. Figure 3d shows the cycling performance of the cell at a current density of 0.1 mA cm^{-2} for 500 h. The initial overpotential of the cell was 26 mV but after 500 cycles the overpotential was slightly increased and reached 34 mV. There was no big difference and fluctuations in the overpotential of the cell, which indicates that the electrolyte can suppress Li dendrite formation for a prolonged duration.

Physical characterization of the cathode material

Figure S8 shows the XRD pattern of NCM811 and 2 mol% $LiNbO_3$ (LNO) coated NCM811 particles, and no phase difference can be observed between the bare and LNO-coated NCM811 cathode particles. The electronic valence state and surface chemical composition of the bare and $LiNbO_3$ coated NCM811 were characterized by XPS analysis and the results are shown in Figure 4, Figure S9, and S10. Figure 4 a–d illustrates the full scan spectrum of bare and 2 mol% LNO-NCM811, which suggests the existence of the elements of Li 1s, Ni 2p, Co 2p, Mn 2p, Nb

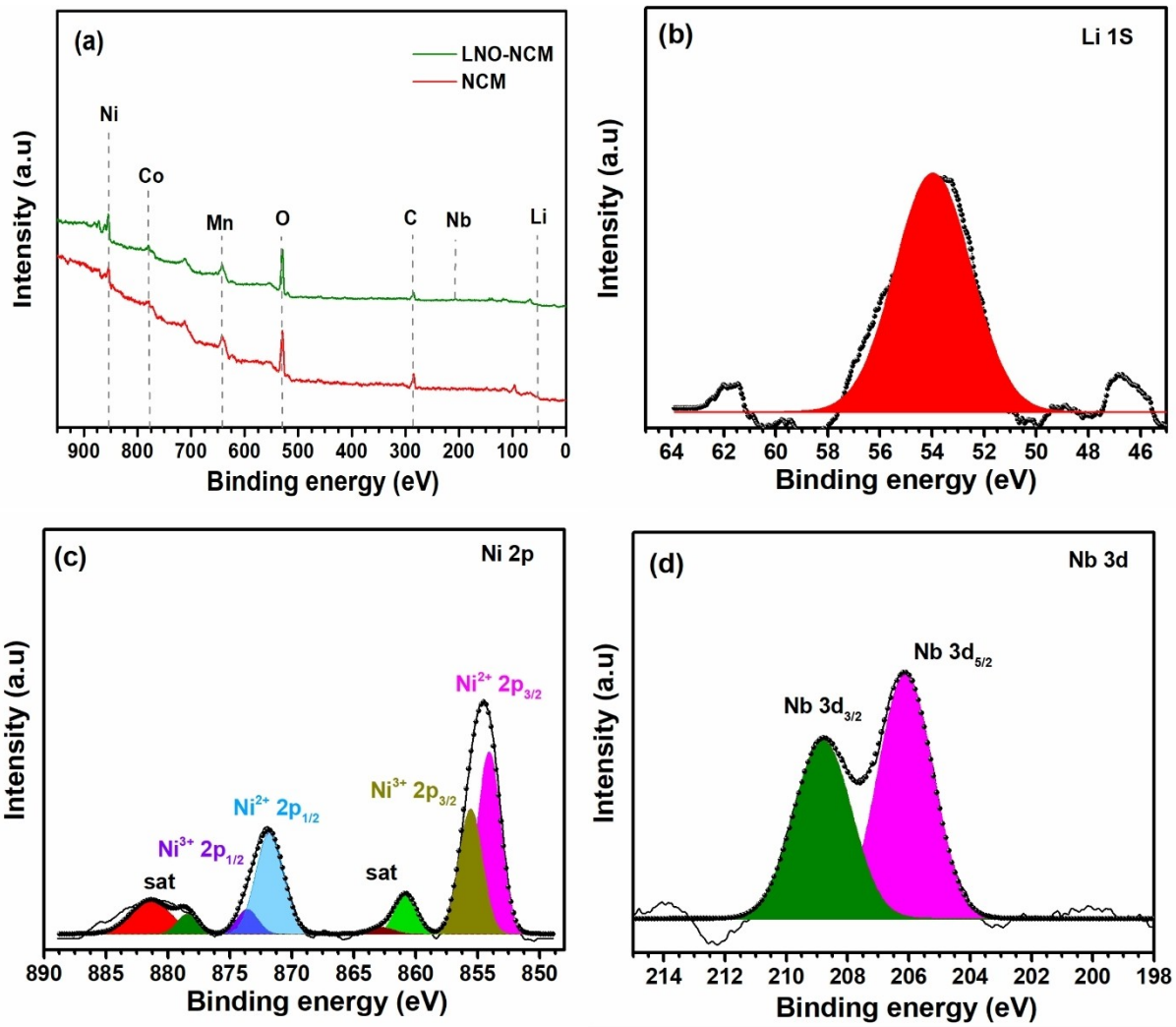

Figure 4. XPS results of the NCM811 and LNO-NCM811 cathode particles. (a) XPS full spectra (b) Li 1s spectra, (c) Ni 2p spectra, and (d) Nb 3d spectra of the LNO-NCM811.

3d, and O 1s. Figure 4b displays the Li 1s spectrum with deconvolution of the peaks that can be detected at 53.96 eV. Figure 4c displays characteristic Ni 2p XPS spectra of 2 mol% LNO- NCM811 in comparison with those of the bare NCM811 material, coupled with fitting patterns based on referred Ni 2p band energies ($Ni^{2+}2p_{1/2}$: 871.76 eV, $Ni^{2+}2p_{3/2}$: 854.07 eV, $Ni^{3+}2p_{1/2}$: 873.58 eV and $Ni^{3+}2p_{3/2}$: 855.56 eV) from the XPS standard reference database (NIST- National Institute of Standards and Technology).[56] The Ni 2p XPS spectra of bare NCM811 were also recorded and studied as shown in Figure S 10b. Figure S 9a represents the deconvoluted spectrum of Co 2p and the two main peak positions at 780.01 and 794.93 eV are assigned to Co $2p_{3/2}$ and Co $2p_{1/2}$, signifying the dominant Co^{3+} cation. Figure S 9b illustrates the deconvoluted spectrum of Mn 2p and the peaks at 641.37 and 653.23 eV confirm the splitting of $Mn2p_{3/2}$ and Mn $2p_{1/2}$, which are consistent with the Mn^{4+} cation.[57] In Figure 4d the Nb $3d_{3/2}$ peak appears at 208.81 eV, while the Nb $3d_{5/2}$ peaks appear at 206.11 eV, indicating clear evidence that $LiNbO_3$ is on the NCM811 particle surface.[58,59] Figures S11 and 5 show the FE-SEM and TEM images of the NCM811 and LNO-coated NCM811 particles. The NCM811 particle has an ellipsoidal morphology, and the primary particle size is in the range of 5–6 μm. After LNO coating, there is not much change from the particle size and the morphology looks the same. The HR-TEM image (Figures 5 c–d) confirms the LNO coating, and the coating layer thickness is found to be 3−5 nm. Nickel (Ni), cobalt (Co), manganese (Mn), and oxygen (O) are uniformly distributed in the NCM811 material, which is evident from the elemental mapping. (Figure S11) According to energy dispersive spectrometry (EDS), elemental mapping confirms that the element Nb is present on the surface of the LNO-coated NCM811 particle. (Figure 5)

Conventional Li-metal battery (LMB)

Figure S12 shows the charge-discharge performance, cycle life, and rate capability of the NCM811 cathode-based Li-metal

Research Article
doi.org/10.1002/celc.202200317

Chemistry Europe
European Chemical Societies Publishing

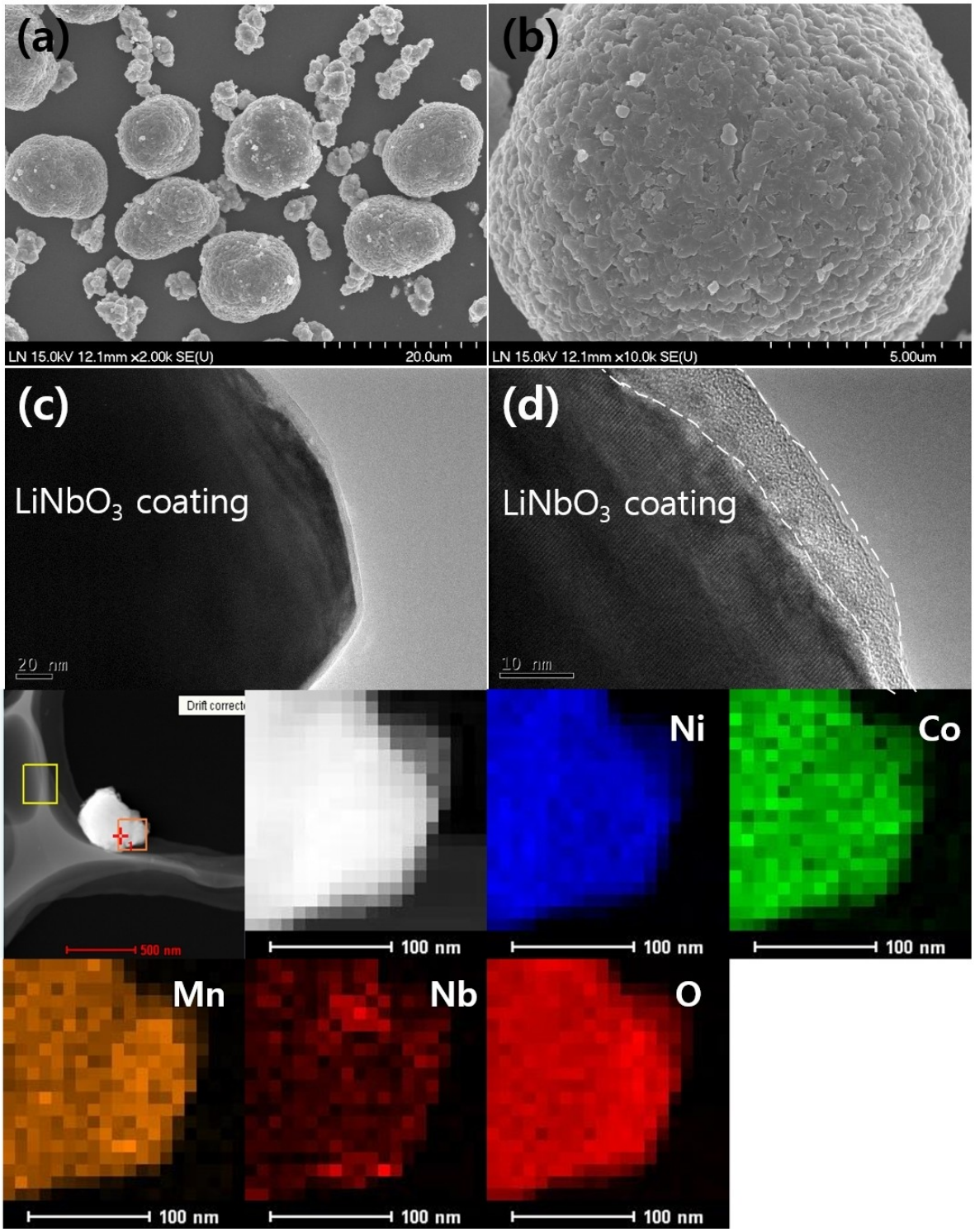

Figure 5. $LiNbO_3$ coated NCM811 (a, b) SEM image, (c, d) TEM image and EDS mapping image of the $LiNbO_3$ coated NCM811 particle.

battery at 25 °C using the liquid electrolyte. The characteristic curve confirms Li-deintercalation/intercalation during the charge/discharge process of the cathode. The electrochemical reaction can be explained as follows:

During the charging process (de-intercalation)

$$LiNi_{0.8}Co_{0.1}Mn_{0.1}O_2 \rightarrow Li_{1-x}Ni_{0.8}Co_{0.1}Mn_{0.1}O_2 + x\ Li^+ + x\ e^- \quad (1)$$

During the discharging process (intercalation)

$$Li_{1-x}Ni_{0.8}Co_{0.1}Mn_{0.1}O_2 + x\ Li^+ + x\ e^- \rightarrow LiNi_{0.8}Co_{0.1}Mn_{0.1}O_2 \quad (2)$$

The charge-discharge voltage plateaus are positioned at around 3.84, 4.25 V *vs.* Li/Li^+, and 3.8, 4.23 V *vs.* Li/Li^+, respectively, and correspond to the redox reactions of Ni^{2+}/Ni^{4+} and Co^{3+}/Co^{4+} in NCM811. The NCM811 cell shows an initial charge, and discharge capacity of 226 and 174 mAh g^{-1}, respectively, at a rate of 0.2 C with a Coulombic efficiency of 77% (1 C = 180 mAh g^{-1}). A marginal increase in the capacity profile is noted; for example, at the 12th cycle, the capacity reached the maximum value of 189 mAh g^{-1} owing to a slower activation of the cathode. After 100 cycles, the bare NCM811 cell retained a discharge capacity of 184 mAh g^{-1}, which corresponds to a retention rate of 97.3%. After the LNO coating, the NCM811 displayed an initial charge and discharge capacity of 237 and 197 mAh g^{-1}, respectively, with a Coulombic efficiency of 83%. The observed reversibility is much better than for pristine NCM811. After 100 cycles, the cell maintained a discharge capacity of 209 mAh g^1 (Figures S13 a–b). The rate performance of the two cells was studied at the rates of 0.1 to 1 C. Figures S12 c−d show the NCM811 rate performance for various current rates. Apparently, at high C rates, the capacity of the cell is decreased due to slow ionic motion within the electrode and at the electrode/electrolyte interface and therefore it takes long for the charge distribution to reach the equilibrium state. In contrast, the LNO-coated NCM811 cell exhibits a significantly improved discharge capacity, and rate capability at high C rates (Figures S13 c–d). We believe the superior performance in terms of discharge capacity, rate performances, and cycle life is mainly because of the LNO modification over the active material of the cathode. For comparison, the prepared 5 and 10 mol% of LNO-coated NCM811 liquid cell electrochemical performance are shown in Figure S14. The initial charge and discharge capacities of the 5 and 10 mol% of LNO-coated NCM811 cells are 213/192 and 200/179 mAh g^{-1} and the corresponding coulombic efficiency are 89.8 and 89.5%. After a few cycles, the capacity of the cells is decreased due to the Li-ion irreversibility and high resistance of the cell. Compare to the 2 mol% LNO coated cell, the capacity of the thick (5 and 10 mol%) LNO coated layer NCM811 cells are decreased due to the Li-ion transfer suppression in the $LiNbO_3$ and NCM811 interface.

All Solid-state Li-metal Battery (ASSLMB)

For comparison, the NCM811 cathode in ASSLMB is tested at 25 °C. The initial discharge capacity is 51 mAh g^{-1}; after 50 cycles, the discharge capacity reached 30 mAh g^{-1} (Figure S15). At 25 °C, the solid-state Li-metal Battery (SSLMB) provided a low discharge capacity due to the low ionic conductivity and poor interface contact between the electrode and electrolyte. Figure S16 shows the electrochemical impedance spectra (EIS) of the Li||S3||NCM811 cell. The charge transfer resistance of the NCM811 cathode cell is 228 Ω and it indicates a sluggish Li-ion transfer in the interface. Therefore, we were testing at 60 °C to further enhance the electrochemical performance of the cell. The succinonitrile is melting at 58.67 °C, so it additionally helps to enhance the electrochemical performance of the cell at 60 °C (Figure S17). To further understand the feasibility of using an LNO-coated NCM811 cathode in ASSLMB, samples were fabricated and compared with NCM811 in the potential range of 2.8–4.3 V at 60 °C, which is shown in Figures 6 a–d and 7 a–d. NCM811-based cells provide an initial charge and discharge capacity of 186 and 163 mAh g^{-1}, respectively, and exhibit a Coulombic efficiency of 87%. After 100 cycles, the discharge capacity decreased to 113 mAh g^{-1} and state-of-health is 69.3%. Therefore, the complex nature of ion transport between the cathode and solid electrolyte interface increases problems in Li-ion deficiency and contact loss for the ionic diffusion path. In contrast, the Li-ion-based coating layer strategy tuning of the interface enhances the ionic mobility in the region. Also, LNO-coated NCM811 with metallic Li affords an initial charge and discharge capacity of 205 and 198 mAh g^{-1}, respectively, with a Coulombic efficiency of 97%. The cell retains its discharge capacity of 141 mAh g^{-1} and the state-of-health is 71.2% after 100 cycles. We compare the present work with previously reported high voltage cathode based SSB in Table 2.[1,5,20,22,25,27,28,33,42,60–63] The rate capabilities of NCM811 and LNO-NCM811 SSB are also studied between a 0.1 to 1 C rates to further understand the role of the LNO coating. Figures 6 (c–d) show the rate capability curve of the NCM811 cathode-based SSB in a voltage range of 2.8–4.3 V at different C rates. Figures 7 c–d illustrate the rate performance of an LNO-NCM811 cathode-based SSB at different C rates. Noticeably, the bare NCM811 cathode-based SSB suffers from contact loss with the cathode active material, irreversibility of de-intercalated Li-ions, and thus, Li-ion reduction at the interface. In contrast, the excellent discharge capacity, Coulombic efficiency, and state-of-health of an LNO-coated NCM811 cathode cell are caused by the LNO buffer layer stabilizing the interface between the LNO-NCM811 cathode and the CSE electrolyte.[38,64] It can be concluded that LNO coating not only improves the point contact between the cathode particles and the electrolyte, but also leads to increases in the mobility of the Li-ions across the interface. Figure S18 shows the electrochemical impedance spectra (EIS) of the Li||S3||NCM811 and Li||S3||LNO-NCM811 cells. The charge transfer resistance of the NCM811 cathode cell is 60.46 Ω but after the LNO coating, the resistance of the LNO-NCM811 cell decreased to 44.01 Ω. It indicates that surface modification improves the smooth Li-ion transfer in the interface. The LNO coating decreases the charge-transfer resistance but the discharge capacity and rate performance of SSB are still limited compared with those of liquid cells. In conventional liquid electrolytes, contact loss is not a significant problem because of the wettability nature and the presence of more mobile Li-ions in the electrolyte. Figure 8a shows the electrochemical performance of an NCM cathode-based SSB, which has a higher possibility of particle-particle contact loss and Li-ion reduction on the surface and interface of the active material. After LNO modification, the movements of Li-ions across the NCM particle surface and interface are common; consequently, the discharge capacity is high, but a minor contact loss is inevitable. [Figure 8b] The surface morphology of the LNO coated NCM811 cathode electrode was studied to understand the capacity loss mechanism of the SSB. Figure S19

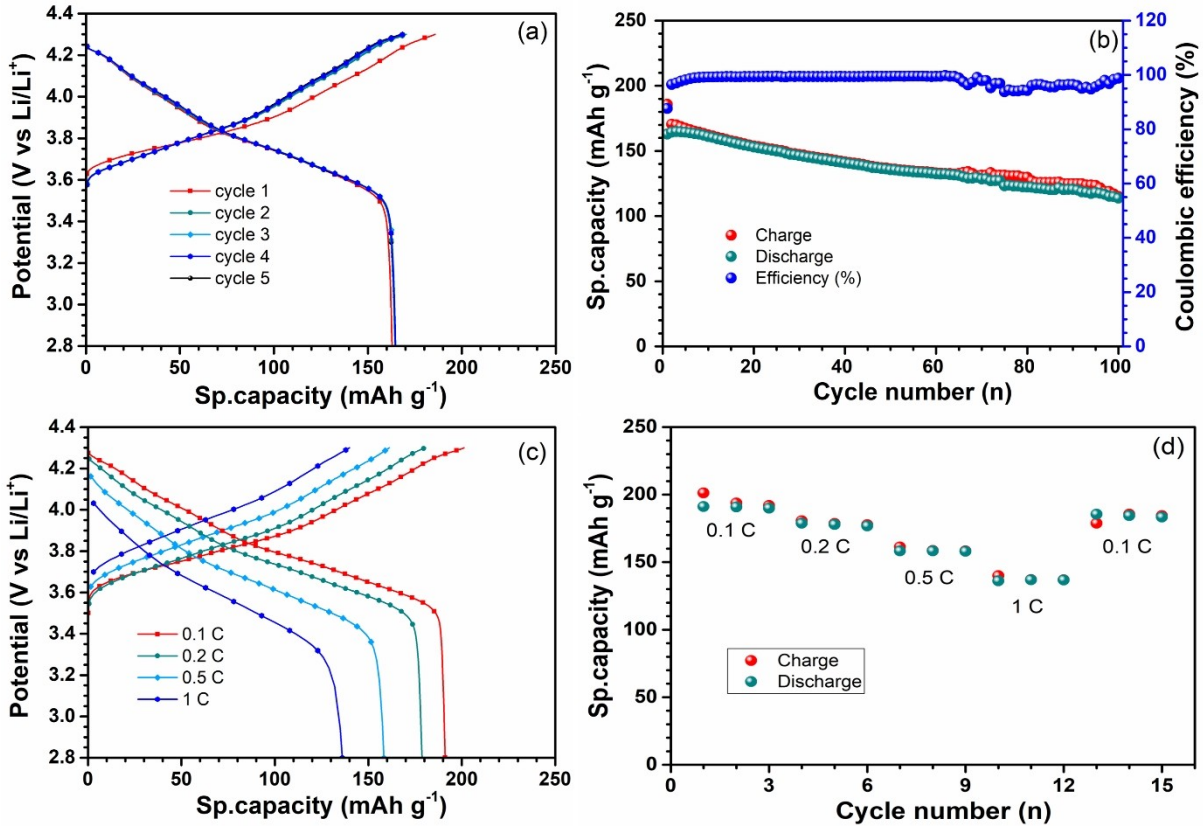

Figure 6. Li||CSE (S3)||NCM811 cell electrochemical performance. (a) First, 5 cycles of the charge/discharge performance, (b) cycle life of the cell at 0.2 C rate, (c) charge/discharge curve, and (d) cycle life of the cell at different C rates. The electrochemical performance was studied at 60 °C.

Table 2. Comparison of previously reported work with our study.

Electrolyte	Cathode	Current density & operating Temperature	Discharge capacity [mAh g^{-1}]	Potential window *vs* Li/Li$^+$	Ref
Our electrolyte	$LiNi_{0.8}Co_{0.1}Mn_{0.1}O_2$& $LiNbO_3$@ $LiNi_{0.8}Co_{0.1}Mn_{0.1}O_2$	0.1 C and 60 °C	191 mAh g^{-1} & 202 mAh g^{-1}	2.8–4.3 V	this work
PVA/PAN/LiTFSI/LATP/SN	$LiFePO_4$	0.1 C and RT	156.9 mAh g^{-1}	2–4 V	1
PEO/LLZO/LiTFSI	$LiFePO_4$	0.1 C and 55 °C	155.8 mAh g^{-1}	2.5–3.85 V	5
LLZTO/PVDF-HFP/ PEO/LiTFSI	$LiFePO_4$	0.1 C and 60 °C	141.2 mAh g^{-1}	2.7–3.8 V	20
PVDF-HFP/LAGP/LiTFSI	$LiFePO_4$	0.1 C and RT	154.06 mAh g^{-1}	2.7–3.85 V	22
PVDF-HFP/10 wt% m-SBA15 + 1 M $LiPF_6$ (EC/DEC)	$LiNi_{0.5}Co_{0.2}Mn_{0.3}O_2$	0.1 C and 25 °C	194 mAh g^{-1}	2.5–4.3 V	25
PVDF-HFP/LLZTO/LiTFSI	$LiFePO_4$	0.1 C and RT	152.1 mAh g^{-1}	2.7–4.2 V	27
LLZTO/PVDF-HFP/ LiTFSI/SN + Liquid Electrolyte	$LiFePO_4$	0.1 C and RT	157.8 mAh g^{-1}	2.6–4 V	28
PVDF-HFP/LiTFSI/LATP/SN	$LiFePO_4$	0.1 C and 25 °C	168.4 mAh g^{-1}	2.8–4.2 V	33
PVDF/PAN/Al-LLZO/$LiClO_4$/SN	$LiNi_{0.8}Co_{0.1}Mn_{0.1}O_2$	0.1 C and RT	160.92 mAh g^{-1}	2.6–4.2 V	42
Tri-CPE (PVDF/PAN)	$LiNi_{0.8}Co_{0.1}Mn_{0.1}O_2$	0.1 C and 25 °C	171.4 mAh g^{-1}	2.7–4.2 V	60
PVDF-HFP/LLZO + 1 M LiTFSI in TEGDME	$LiFePO_4$	0.1 C and RT	140 mAh g^{-1}	3–3.8 V	61
BStSi solid electrolyte	$LiNi_{0.8}Co_{0.1}Mn_{0.1}O_2$	0.1 C and 0 °C	126 mAh g^{-1}	2.8–4.2 V	62
PEO + LiTFSI + Wheat flour electrolyte	$LiNi_{0.8}Co_{0.1}Mn_{0.1}O_2$	0.1 C and 25 °C	133 mAh g^{-1}	2.5–4.2 V	63

shows the SEM images of LNO-NCM811 particles after 100 cycles under a 0.2 C rate between 2.8–4.3 V. After long cycling, small cracks were formed on the surface of the particles. The cracks formed on the surface of the electrode materials because of the volume expansion. The lithium-ion irreversibility of the cell was caused by the broken particles, which further leads to capacity loss. However, to further increase the cycle life and discharge capacity of ASSLMB, using highly conductive coating materials over the active material and self-healing polymers as electrolytes are good options, which are being considered in our ongoing studies.

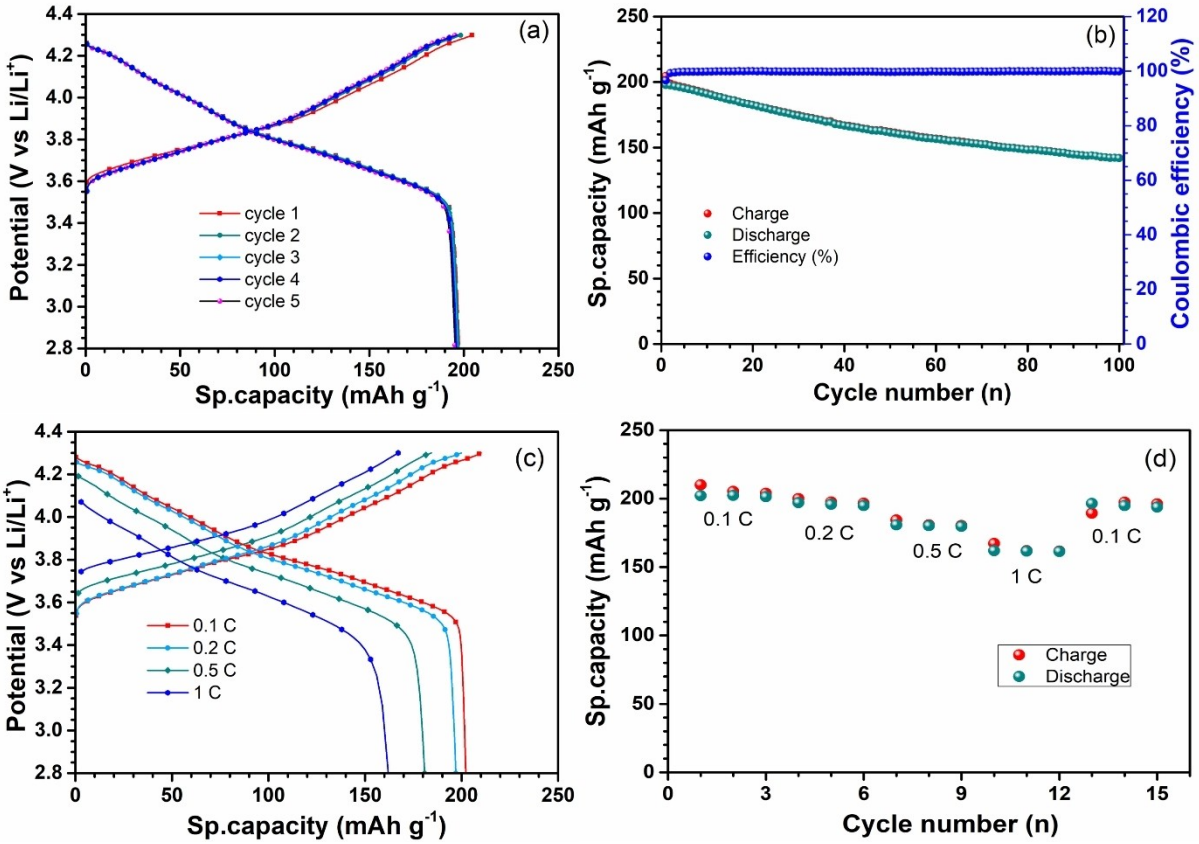

Figure 7. Li||CSE (S3)||LNO@NCM811 cell electrochemical performance. (a) First, 5 cycles of the charge/discharge performance, (b) cycle life of the cell at 0.2 C rate, (c) charge/discharge curve, and (d) cycle life of the cell at different C rates. The electrochemical performance was studied at 60 °C.

Conclusion

Novel liquid-free PVDF-HPF/LLZO CSEs were prepared by the solution casting method. The optimized CSE provides a high ionic conductivity of 4.23×10^{-4} and 8.14×10^{-4} S cm^{-1} at 25 and 60 °C, respectively, with an electrochemical stability up to 4.76 V *vs.* Li/Li^{+}. Similarly, the cathode NCM 811 was modified with a $LiNbO_3$ coating to improve the cathode-electrolyte interphase. The electrochemical study displays that the LNO-NCM811 cathode in the liquid electrolyte provides a high discharge capacity and excellent rate capability at various C rates compared with the pristine cathode a 25 °C. After surface modification, the LNO-NCM811 cathode-based SSB assembly provides a high discharge capacity of 198 mAh g^{-1} and a state-of-health of 71.2% using CSE. The $LiNbO_3$ buffer layer certainly improves the interfacial contact between the cathode and the electrolyte and reduces the interfacial resistance. The Li-ion-based coating layer is an excellent alternative for enhancing the initial charge/discharge capacity and rate performance and reducing Li-ion depletion across the interface.

Experimental Section

Preparation of Composite solid electrolyte (CSE)

Garnet type $Li_7La_3Zr_2O_{12}$, LLZO ceramic powder was acquired from Jeong Kwan Co. Ltd. and stored in an Argon-filled glovebox. CSEs were prepared by the solution casting method. PVDF-HFP, 30% LiTFSI, and various ratios (0, 10, 20, 30, and 40 wt.%) of SN were dissolved in N, N-dimethylformamide (DMF) at 40 °C. The resulting solution was stirred well until the formation of a clear homogeneous solution. (Table S1) Afterward, 10 wt.% of LLZO ceramic powder was added to the solution. Subsequently, the viscous solution was casted onto the Mylar sheet and heated to 60 °C for 24 h in a vacuum oven to remove any remaining solvent. The CSE film was cut to an appropriate size (diameter 1.8 cm) for further characterization and electrochemical studies. (Figure 1a)

Preparation of $LiNbO_3$-coated NCM811 particles

NCM811 active material was purchased from Wellcoss Corporation Pvt Ltd. and used as received. $LiNbO_3$ was coated onto the surface of NCM811 by the sol-gel method. In a typical process, lithium niobium ethoxide (2 mol.%) was dissolved in 2-propanol. Then, the appropriate amount of NCM811 particles was dispersed in the solution by ultra-sonication for 1 h. Afterwards, the solution was continuously stirred until evaporation of the solvent at 60 °C. Finally, the powder was calcined at 400 °C for 1 h under an oxygen (O_2) atmosphere to prepare the 2 mol%-$LiNbO_3$ coated NCM811 particle.

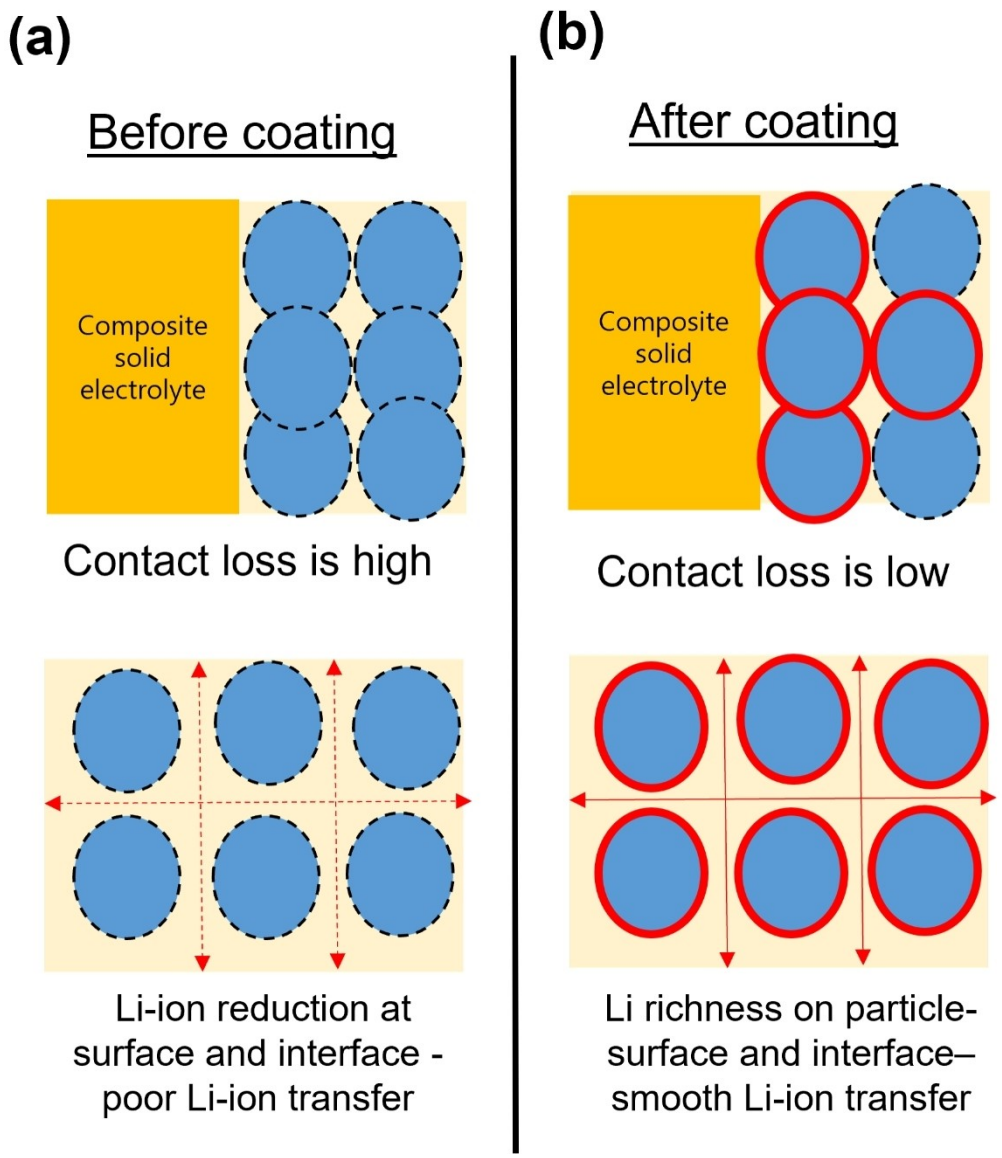

Figure 8. Schematic illustrations of the Li-ion concentration in the cathode particle-particle interface. (a) NCM811 cell contact loss and Li-ion reduction at the interface and (b) LNO-NCM811 cell contact loss and smooth Li-ion transfer.

Characterization of the samples

The crystal structure of the samples was analyzed using a high-resolution X-ray diffractometer (HR-XRD, Rigaku, Japan, D/MAX Ultima III) under 40 kV/40 mA. The functional groups of the samples were studied through Fourier-transform infrared spectroscopy (FT-IR, Shimadzu, and IRPresitge-21 - Japan). The surface morphology, elemental composition, and internal structure of the samples were studied using a Field emission-scanning electron microscopy and energy dispersive X-ray spectroscopy (FE-SEM/EDX–S-4700/EX-200), and high resolution-transmission electron microscopy (HR-TEM; JEM-2000, EX-II, JEOL, Japan). Thermogravimetric analysis (GA-Shimadzu, Japan, and TGA-50) was conducted in the temperature range of 25−800 °C under N_2 atmosphere (5 °C min^{-1}).

Solid-state battery (SSB) preparation

Electrochemical impedance spectroscopy (EIS) was used to evaluate the ionic conductivity of the SS||CSE||SS cell in the frequency range of 1 kHz−1 Hz with a potential amplitude of 10 mV using a Bio-logic VSP potentiostat. Furthermore, the temperature dependence of the Li-ion conductivity of CSE was measured in the range of 25–80 °C. The linear sweep voltammetry (LSV) of the CSEs was tested using an asymmetric cell (Li||CSE||SS) at a scan rate of 1 mV s^{-1} in the potential range 0−5 V (Biologic, Model VSP France). The Li||CSE||Li-symmetric cell was also assembled using a 2032 coin-cell and the performance was studied galvanostatically at a current density of 0.1 mA cm^{-2}. The chronoamperometry (CA) test for the Li-ion transference number calculation of the Li-symmetric cell was tested at the applied voltage of 10 mV. The SSB comprised an NCM811 or LNO-NCM811 cathode and Li metal foil as an anode. The NCM811 active material was collected from Wellcoss Corporation Ltd. and used as received. For the cathode slurry preparation, NCM811 powder or $LiNbO_3$-NCM811, CSE, PVDF, and Super

(84:10:4:2 weight ratio) were mixed in a N-Methyl-2-pyrrolidone (NMP) solvent and cast onto the surface of an Al-foil. Then, the slurry was heated to 120 °C for 12 h to remove any remaining solvent. The active material loading of the prepared cathode was in the range of 3.5–4 mg and the diameter of the electrode was 1.4 cm. For cell assembly, the cathode (NCM811 or LNO-NCM811) was attached to both sides of the CSE (see Figure 1b). The charge-discharge performance was studied in the voltage range of 2.8–4.3 V at 60 °C. Before the electrochemical study, the cell was heated to 60 °C for 24 h to increase the interfacial contact between the electrode-electrolyte. For comparison, we made a liquid cell using 1 M $LiPF_6$ in ethylene carbonate (EC)/dimethyl carbonate (DMC) (1:1 volume ratio solvent) as an electrolyte. The electrochemical performance of the cell was studied at 25 °C. III PNE power and energy solution (Korea) were used to analyze the charge-discharge performance of the electrochemical cell.

Acknowledgements

The author would like to thank Jeong Kwan.Co. Ltd for their consistent support. This work was supported by the National Research Foundation of Korea (NRF) grant funded by the Korean government (Ministry of Science, ICT & Future Planning) (No. 2019R1A2C1007620). VA acknowledges financial support from the Science and Engineering Research Board (SERB), a statutory body of Department of Science & Technology, Govt. of India, through Swarnajayanti Fellowship (SB/SJF/2020-21/12).

Conflict of Interest

The authors declare no conflict of interest.

Data Availability Statement

Research data are not shared.

Keywords: Composite solid electrolytes · High voltage cathode · Plasticizer · Solid-state battery · Surface coating

[1] H. K. Tran, Y. S. Wu, W. C. Chien, S. H. Wu, R. Jose, S. J. Lue, C. C. Yang, *ACS Appl. Energ. Mater.* **2020**, *3*, 11024–11035.
[2] M. Zhao, Y. Xu, P. Ren, Y. Zuo, W. Su, Y. Tang, *Dalton Trans.* **2020**, *49*, 2933–2940.
[3] B. Ramkumar, S. Yuvaraj, S. Surendran, K. Pandi, H. V. Ramasamy, Y. S. Lee, R. K. Selvan, *J. Phys. Chem. Solids.* **2018**, *112*, 270–279.
[4] S. B. Lee, B. Ramkumar, *J. Ind. Eng. Chem.* **2022**, *110*,262–273.
[5] H. Zhuang, W. Ma, J. Xie, X. Liu, B. Li, Y. Jiang, S. Huang, Z. chen, B. Zhao, *J. Alloys Compd.* **2021**, *860*, 157915.
[6] W. Zha, W. Li, Y. Ruan, J. Wang, Z. Wen, *Energy Storage Mater.* **2021**, *36*, 171–178.
[7] S. P. Culver, R. Koerver, T. Krauskopf, W. G. Zeier, *Chem. Mater.* **2018**, *30*, 4179–4192.
[8] D. Cao, X. Sun, Q. Li, A. Natan, P. Xiang, H. Zhu, *Matter.* **2020**, *3*, 1, 57–94.
[9] X. Shen, R. Zhang, X. Chen, X. B. Cheng, X. Li, Q. Zhang, *Adv. Energy Mater.* **2020**, *10*, 1.
[10] T. Famprikis, P. Canepa, J. A. Dawson, M. S. Islam, C. Masquelier, *Nat. Mater.* **2019**, *18*, 1278–1291.
[11] E. A. Wu, S. Banerjee, H. Tang, P. M. Richardson, J. M. Doux, J. Qi, Z. Zhu, A. Grenier, Y. Li, E. Zhao, G. Deysher, E. Sebti, H. Jguyen, R. Stephens, G. Verbist, K. W. Chapman, R. J. Clement, A. Banerjee, Y. S. Meng, S. P. Ong, *Nat. Commun.* **2021**, *12*, 1256.
[12] K. Nie, Y. Hong, J. Qiu, Q. Li, X. Yu, H. Li, L. Chen, *Front. Chem.* **2018**, *6*, 616.
[13] R. Murugan, V. Thangadurai, W. Weppner, *Angew. Chem. Int. Ed.* **2007**, *46*, 7778–7781; *Angew. Chem.* **2007**, *119*, 7925–7928.
[14] N. J. J. De Klerk, I. Rosłoń, M. Wagemaker, *Chem. Mater.* **2016**, *28*, 7955–7963.
[15] B. Ramkumar, K. So-young, N. Chan-woo, V. Aravindan, L. Yun-Sung, *Electrochim. Acta* **2020**, *359*, 136955.
[16] B. Ramkumar, N. Chan-woo, V. Aravindan, D. Eum, K. Kang, Y. S. Lee, *ChemElectroChem* **2021**, *8*, 570–576.
[17] G. Vardar, W. J. Bowman, Q. Lu, J. Wang, R. J. Chater, A. Agudero, R. Seibert, J. Terry, A. Hunt, I. Waluyo, D. D. Fong, A. Jarry, E. J. Crumlin, S. L. Hellstrom, Y. M. Chiang, B. Yildiz, *Chem. Mater.* **2018**, *30*, 6259–6276.
[18] A. Banerjee, X. Wang, C. Fang, E. A. Wu, Y. S. Meng, *Chem. Rev.* **2020**, *120*, 6878–6933.
[19] Q. Yi, W. Zhang, S. Li, X. Li, C. Sun, *ACS Appl. Mater. Interfaces* **2018**, *10*, 35039–35046.
[20] J. Huang, Y. Huang, Z. Zhang, H. Gao, C. Li, *Energy Fuels* **2020**, *34*, 15011–15018.
[21] Y. Li, H. Wang, *Ind. Eng. Chem. Res.* **2021**, *60*, 1494–1500.
[22] Q. Guo, Y. Han, H. Wang, S. Xiong, Y. Li, S. Liu, K. Xie, *ACS Appl. Mater. Interfaces* **2017**, *9*, 41837–41844.
[23] Z. Li, H. M. Huang, J. K. Zhu, J. F. Wu, H. Yang, L. Wei, X. Guo, *ACS Appl. Mater. Interfaces* **2019**, *11*, 784–791.
[24] N. Meng, X. Zhu, F. Lian, *Particuology* **2021**, *60*, 14–36.
[25] C. C. Yang, Z. Y. Lian, S. J. Lin, J. Y. Shih, W. H. Chen, *Electrochim. Acta* **2014**, *134*, 258–265.
[26] M. Ulaganathan, C. M. Mathew, S. Rajendran, *Electrochim. Acta* **2013**, *93*, 230–235.
[27] J. Lu, Y. Liu, P. Yao, Z. Ding, Q. Tang, J. Wu, Z. Ye, K. Huang, X. Liu, *Chem. Eng. J.* **2019**, *367*, 230–238.
[28] T. Wei, Z. H. Zhang, Z. M. Wang, Q. Zhang, Y. S. Ye, J. H. Lu, Z. U. Rahman, Z. W. Zhang, *ACS Appl. Energ. Mater.* **2020**, *3*, 9428–9435.
[29] Z. Xue, D. He, X. Xie J Mater, *Chem* **2015**, *3*, 19218–19253.
[30] W. Zha, F. Chen, D. Yang, Q. Shen, L. Zhang, *J. Power Sources.* **2018**,397,87–94.
[31] L. Z. Fan, J. Maier, *Electrochem. Commun.* **2006**, *8*, 1753–1756.
[32] M. Echeverri, N. Kim, T. Kyu, *Macromolecules.* **2012**, *45*, 6068–6077.
[33] J. Gai, F. Ma, Z. Zhang, D. Sun, Y. Jin, Y. Guo, W. Kim, *ACS Sustainable Chem. Eng.* **2019**, *7*, 15896–15903.
[34] W. Zhang, X. Wang, Q. Zhang, L. Wang, Z. Xu, Y. Li, S. Huang, *ACS Appl. Energ. Mater.* **2020**, *3*, 5238–5246.
[35] X. Li, K. Zhang, M. Wang, Y. Liu, M. Qu, W. Zhao, J. Zheng, *Sustain. Energy Fuels* **2018**, *2*, 413–421.
[36] H. J. Noh, S. Youn, C. S. Yoon, Y. K. Sun, *J. Power Sources* **2013**, *233*, 121–130.
[37] P. Hou, J. Yin, M. Ding, J. Huang, X. Xu, *Small.* **2017**, *13*, 1–29.
[38] X. Li, L. Jin, D. Song, H. Zhang, X. Shi, Z. Wang, L. Zhang, L. Zhu, *J. Energy Chem.* **2020**, *40*, 39–45.
[39] Y. J. Kim, R. Rajagopal, S. Kang, K. S. Ryu, *Chem. Eng. J.* **2020**, *386*, 123975.
[40] Z. Chen, D. Chao, J. Lin, Z. Shen, *Mater. Res. Bull.* **2017**, *96*, 491–502.
[41] D. Mazza, *Mater. Lett.* **1988**, *7*, 205–207.
[42] S. L. Beshahwured, Y. S. Wu, S. H. Wu, W. C. Chien, R. Jose, S. J. Lue, C. C. Yang, *Electrochim. Acta* **2021**, *366*, 137348.
[43] Shalu, V. K. Singh, R. K. Singh, *J. Mater. Chem. C.* **2015**, *3*, 7305–7318.
[44] Shalu, S. K. Chaurasia, R. K. Singh, S. Chandra, *J. Appl. Polym. Sci.* **2015**, *132*, 41456.
[45] M. Celik, A. Kızılaslan, M. Can, T. Cetinkaya, H. Akbulut, *Electrochim. Acta* **2021**, *371*, 137824.
[46] N. Mozhzhukhina, A. Y. Tesio, L. P. M. De Leo, E. J. Calvo, *J. Electrochem. Soc.* **2017**, *164*, A518-A523.
[47] D. L. Pavia, G. M. Lampman, G. S. Kriz, J. R. Vyvyan, Introduction to spectroscopy, fourth ed., Brooks/cole cemgage learning, united state of america, (**2008**), 14–106.
[48] S. Abbrent, S. Greenbaum, *Curr. Opin. Colloid Interface Sci.* **2013**, *18*, 228–244.
[49] D. Saikia, Y. W. Chen-Yang, Y. T. Chen, Y. K. Li, S. I. Lin, *Electrochim. Acta* **2009**, *54*, 1218–1227.

[50] C. Fu, Y. Ma, S. Lou, C. Cui, L. Xiang, W. Zhao, P. Zuo, J. Wang, Y. Gao, G. Yin, *J. Mater. Chem. A* **2020**, *8*, 2066–2073.
[51] M. Kerner, N. Plylahan, J. Scheers, P. Johansson, *RSC Adv.* **2016**, *6*, 23327–23334.
[52] J. Liu, Z. Khanam, R. Muchakayala, S. Song, *J. Mater. Sci. Mater. Electron.* **2020**, *31*, 6160.
[53] J. Amici, M. Alidoost, C. Francia, S. Bodoardo, S. M. Crespiera, D. Amantia, M. Biasizzo, F. Caldera, F. Trotta, *Chem. Commun.* **2016**, *52*, 13683–13686.
[54] P. J. Alarco, Y. Abu-Lebdeh, A. Abouimrane, M. Armand, *Nat. Mater.* **2004**, *3*, 476–481.
[55] S. A. Suthanthiraraj, M. K. Vadivel, *Appl Nanosci.* **2012**, *2*, 239–246.
[56] X. Huang, W. Zhu, J. Yao, L. Bu, X. Li, K. Tian, H. Lu, C. Quan, S. Xu, K. Xu, Z. Jiang, X. Zhang, L. Gao, J. Zhao, *J. Mater. Chem. A* **2020**, *8*,17429–17441.
[57] H. K. Kim, H. S. Kang, P. Santhoshkumar, J. W. Park, C. W. Ho, G. S. Sim, C. W. Lee, *RSC Adv.* **2021**, *11*, 21685–21694.
[58] H. Kim, D. Byun, W. Chang, H. G. Jung, W. Choi, *J. Mater. Chem. A.* **2017**, *5*, 25077–25089.
[59] F. Tian, Y. Zhang, Z. Liu, R. D. S. Monteiro, R. M. Ribas, P. Gao, Y. Zhu, H. Yu, L. Ben, X. Huang, *Solid State Ionics.* **2021**, *359*,115520.
[60] K. Z. Walle, L. M. Babulal, S. H. Wu, W. C. Chien, R. Jose, S. J. Lue, J. K. Chang, C. C. Yang, *ACS Appl. Mater. Interfaces* **2021**, *13*,2507–2520.
[61] W. Zhang, J. Nie, F. Li, Z. L. Wang, C. Sun, *Nano Energy* **2018**, *45*, 413–419.
[62] Z. Lin, J. Liu, *RSC Adv.* **2019**, *9*, 34601–34606.
[63] Y. Lin, Y. Cheng, J. Li, J. D. Miller, J. Liu, X. Wang, *RSC Adv.* **2017**, *7*, 24856–24863.
[64] J. Haruyama, S. Keitaro, H. Liyuan, T. Kazunori, T. Yoshitaka, *Chem. Mater.* **2014**, *26*, 4248–4255.

Manuscript received: March 27, 2022
Revised manuscript received: June 14, 2022
Accepted manuscript online: June 15, 2022